Applied Mathematical Modelling 154 (2026) 116672

Contents lists available at ScienceDirect

Applied Mathematical Modelling

journal homepage: www.elsevier.com/locate/apm

Lagrange multiplier and penalty methods for the thermal buckling analysis of higher-order composite laminates

Saeedeh Qaderi [a], Nicholas Fantuzzi [a,*], J.N. Reddy [b]

[a] DICAM Department, University of Bologna, Bologna, Italy
[b] Department of Mechanical Engineering, Texas A&M University, College Station, Texas, USA

ARTICLE INFO

Editor: Johann Sienz

Keywords:
FEM
Buckling
GPLRC plate
Lagrange multiplier method
Penalty method

ABSTRACT

Advances in composite structures with improved mechanical properties enable a better balance between strength and weight, benefiting high-demand fields like civil and aerospace engineering. Higher-order theories effectively model such structures but are often complex owing to the multitude of parameters involved. To ease this burden, internal constraints are introduced, but they can complicate numerical methods like the finite element method (FEM) by requiring higher-order shape functions. Driven by the challenges of finite element modeling for constrained composites, this study focuses on the thermal buckling behavior of higher-order GPLRC plates. Internal constraints in higher-order plate theories are introduced by employing the Lagrange Multiplier Method (LMM) and the Penalty Method (PM). These methods disable the interpolation of displacement parameters using Lagrange shape functions with C^0 continuity, ensuring simple shape functions, a well-posed weak formulation, compatibility with standard FEM software, and avoiding the need for complex formulations in a classical finite element framework. The theoretical formulation of the GPLRC laminate plate is derived based on the General Third-order Shear deformation plate Theory (GTST). The Halpin-Tsai model and rule of mixtures are used to determine the laminated plate material properties. Four GPL distribution patterns across composite layers are analyzed for their impact on laminate buckling behavior. The LMM and PM results are systematically compared by varying parameters such as element count, GPL weight fraction, and geometrical dimensions, demonstrating the effectiveness and accuracy of constraint enforcement techniques in FEM-based thermal buckling analysis of composite plates. The study provides a robust framework for modeling complex composite structures, enabling efficient solutions in computational environments.

1. Introduction

Graphene platelet-reinforced composite (GPLRC) laminates have emerged as promising materials for high-performance applications due to their superior strength-to-weight ratio, thermal stability, and stiffness. These materials are increasingly used in aerospace structures, automotive components, marine systems, and advanced civil infrastructure, where lightweight yet mechanically robust solutions are critical. Accurate modeling of their behavior under various loading conditions, including thermal environments, is essential to ensure safety, durability, and optimal performance in such demanding applications.
Functionally graded graphene platelet reinforced composites (GPLRCs) are promising advanced materials for high-performance

* Corresponding Author.
E-mail addresses: nicholas.fantuzzi@unibo.it (N. Fantuzzi), jnreddy@tamu.edu (J.N. Reddy).

https://doi.org/10.1016/j.apm.2025.116672
Received 13 June 2025; Received in revised form 24 October 2025; Accepted 1 December 2025
Available online 9 December 2025

Nomenclature

a	Length of GPLRC plate
b	Width of GPLRC plate
h	Thickness of GPLRC plate
k	Number of GPLRC Layers
$\circ$	Hadamard Product
n_l	Maximum Number of GPLRC Layers
V^*_{GPL}	Total Volume Fraction of GPLs
W_{GPL}	GPL Weight Fraction
ρ_{GPL}	Mass Density of GPL
ρ	Mass Density of Epoxy
V_{GPL}	Total Volume Fraction of GPLRC
h_k	Thickness of a Single Layer of GPLRC Laminate
p_1–p_2	Penalty Parameters
n	Number of Degrees of Freedom per Node
ΔT	Temperature Variation along GPLRC Plate Thickness
β	Orientation of Layers in Laminated GPLRC Composite
λ	Buckling Mode Eigenvalue
ν	Effective Poisson's Ratio
E	Effective Elasticity Modulus of GPLRC
ρ	Effective Density of GPLRC
α	Effective Thermal Expansion Coefficient of GPLRC
α_0	Normalization Factor
N_{el}	Number of Finite Elements
T	Non-dimensional Critical Buckling Temperature
T_{cr}	Minimum Critical Buckling Temperature

structures due to their excellent thermal [1], mechanical [2,3], and electrical properties [4]. Graphene Platelets (GPLs) and their polymer composites have been extensively studied in terms of their fabrication, functionalization, properties, and applications [5,6]. By tailoring the spatial distribution of GPLs through the thickness of the plate, engineers can achieve optimized structural performance, weight reduction, and resistance to thermal degradation [7]. GPLRC plates are particularly suitable for environments subjected to elevated temperatures, where conventional composites may suffer from thermal instability or reduced load-bearing capacity [8]. Among various structural applications, accurately predicting the thermal buckling behavior of such plates is of significant interest in the design of aerospace panels, automotive components, and microelectromechanical systems (MEMS) [9,10]. Thermal buckling is a critical form of instability resulting from temperature-induced expansion, which can lead to sudden and catastrophic failure if not properly considered during the design phase [11,12]. Moreover, dynamic analysis of GPLRC structures is essential to address various engineering challenges [13]. These materials belong to a broader class of nanostructure reinforced composites, which also includes carbon nanotube (CNT)-reinforced composites. Both GPLRCs and CNT-based composites leverage the exceptional properties of carbon-based nanomaterials to enhance the performance of conventional matrices [14]. Although CNTs have been extensively studied for their exceptional axial stiffness and high aspect ratio, GPLRCs offer advantages such as better dispersion, easier fabrication, and improved interfacial bonding with the matrix [15]. Due to their shared and complementary properties, GPLRCs and CNT-reinforced composites are often grouped as high-performance nano-reinforced composite structures [16,17]. The study of buckling is fundamental in structural engineering, particularly for elements such as columns, beams, and plates, as it offers essential insights into the failure mechanisms of materials and structures [18–20]. Structures can become unstable under certain conditions, resulting in sudden and catastrophic failures due to buckling [21,22]. Consequently, buckling analysis is essential in the design and evaluation of systems subjected to diverse loads and environmental factors [23]. Plus, understanding structural behavior is crucial for optimizing systems [24,25], enhancing engineering performance [26,27], analyzing interaction effects [28], and ensuring compliance with safety standards. Unlike other failure mechanisms, such as material yielding or fracture, buckling can occur under significantly lower loads than those required to cause material failure. This makes buckling analysis an essential component of the design process, enabling engineers to prevent catastrophic failures in structures [29,30], buildings [31], and aerospace components [32,33]. Thermal buckling analysis of composite plates, particularly those incorporating functionally graded or layered GPL distributions, poses significant computational challenges [34], especially when higher-order theories are used to capture transverse shear deformation and warping effects [35]. Moreover, finite element modelling and computational mechanics are broad fields with applications across various domains, including solid mechanics [36], and structural analysis [37]. These disciplines offer powerful tools for analyzing complex physical phenomena in engineering, physics, and the applied sciences. While higher-order displacement theories can improve accuracy, they often result in complex governing equations that require the use of C^1 continuous shape functions in the finite element framework, such as Hermite polynomials [38]. However, the implementation of such shape functions increases the complexity and computational cost of the finite element method (FEM), particularly for multilayered or irregular geometries [39]. The application of Lagrangian multipliers in analyzing composite structures has been extensively investigated in the literature, demonstrating their

robustness and versatility. For instance, Kiani [40] employed the Lagrangian multiplier technique to analyze the free vibration behavior of CNT-reinforced composite plates supported at discrete points, showcasing its effectiveness in handling complex boundary conditions. Similarly, Chen [41] utilized this approach to derive an exact solution to the eigenvalue problem for a clamped orthotropic plate subjected to low-velocity impact, highlighting the method's precision in eigenvalue analysis.

York et al. [42] further extended the analytical framework by incorporating Lagrangian multipliers in the study of skew plates, illustrating its adaptability to non-standard geometries. As emphasized by Berak [43], the Lagrangian multiplier technique can be seamlessly integrated with numerical methods such as finite element analysis (FEA), thereby enhancing its applicability to complex, multilayer, or composite plate systems. Complementing this, the Penalty Method (PM) offers a computationally efficient alternative, particularly beneficial in large-scale simulations where strict enforcement of constraints via Lagrangian multipliers may increase system complexity. Reddy's development of a penalty-based bending element formulation for composite plates [44] exemplifies how LMM and PM contribute significantly to computational methodologies by simplifying implementation of constraints while maintaining acceptable accuracy.

This paper aims to contribute to computational mechanics by introducing a robust and efficient finite element framework for the investigation of the buckling behavior of laminated composite plates. The framework specifically is employed for thermal buckling analysis of graphene platelet-reinforced composite (GPLRC) plates, utilizing General Third-order Shear deformation plate Theory (GTST). Since ensuring inter-element continuity in numerical implementations of higher-order plate theory can be challenging, the Lagrange Multiplier Method (LMM) and the Penalty Method (PM) were employed to enforce the constraints in this work. These two methods allow the formulation to avoid the need for Hermite interpolation functions with C^1 continuity, which simplifies implementation while maintaining the accuracy of higher-order plate theories. Specifically, LMM converts the constrained problem into an augmented system by adding new variables that enforce continuity as equality constraints whereas, regarding the model size, the Penalty Method (PM) does not add any extra degrees of freedom (DOF). Various GPL distribution patterns through the plate thickness are considered to reflect realistic manufacturing and optimize performance. The finite element model is applied to multilayer GPLRC plates under different boundary conditions. A systematic study examines how constraint enforcement methods LMM and PM, GPL dispersion, and plate geometries affect the critical buckling temperature. These findings enhance understanding of advanced composite behavior and promote their wider engineering application.

2. Theoretical background

Consider a laminated GPLRC plate with length a, width b, and thickness h . The plate is modeled using the General Third-Order Shear Deformation Theory (GTST), modified to include the nonlinear von Kármán terms. The plate is composed of k layers, with four different GPL distribution patterns along the thickness, as illustrated in Fig. 1. Displacement fields based on GTST have been presented as [18]:

$$\begin{aligned} u_x(x,y,z) &= u(x,y) + z\theta_x(x,y) + z^3\psi_x(x,y) \\ u_y(x,y,z) &= v(x,y) + z\theta_y(x,y) + z^3\psi_y(x,y) \\ u_z(x,y,z) &= w(x,y) + z^2\phi_z(x,y) \end{aligned} \tag{1}$$

where $u(x,y)$ and $v(x,y)$ are the in-plane-displacements, and $w(x,y)$ is the transverse displacement at the mid-plane z. θ_x and θ_y are the rotations of the mid-plane about the y and x axes, respectively, and ϕ_z is the higher-order term representing thickness stretching (curvature-related field). ψ_x, and ψ_y are warping variables in $x-z$ and $y-z$ planes, respectively. These terms provide a more accurate representation of the plate's behavior than classical plate theories, particularly for thick or composite laminated plates. The strain terms considering von Kármán nonlinearity [45] are:

$$\begin{aligned} \varepsilon_{xx} &= \frac{\partial u}{\partial x} + z\frac{\partial \theta_x}{\partial x} + z^3\frac{\partial \psi_x}{\partial x} + \frac{1}{2}\left(\frac{\partial w}{\partial x}\right)^2 \\ \varepsilon_{yy} &= \frac{\partial v}{\partial y} + z\frac{\partial \theta_y}{\partial y} + z^3\frac{\partial \psi_y}{\partial y} + \frac{1}{2}\left(\frac{\partial w}{\partial y}\right)^2 \\ \varepsilon_{zz} &= 2z\phi_z \\ \gamma_{xy} &= \frac{\partial u}{\partial y} + \frac{\partial v}{\partial x} + z\left(\frac{\partial \theta_x}{\partial y} + \frac{\partial \theta_y}{\partial x}\right) + z^3\left(\frac{\partial \psi_x}{\partial y} + \frac{\partial \psi_y}{\partial x}\right) + \frac{\partial w}{\partial x}\frac{\partial w}{\partial y} \\ \gamma_{yz} &= \frac{\partial w}{\partial y} + \theta_y + z^2\left(3\psi_y + \frac{\partial \phi_z}{\partial y}\right) \\ \gamma_{xz} &= \frac{\partial w}{\partial x} + \theta_x + z^2\left(3\psi_x + \frac{\partial \phi_z}{\partial x}\right) \end{aligned} \tag{2}$$

where $\gamma_{ij} = 2\varepsilon_{ij}$ for $i,j = x,y,z$ and $i \neq j$.

The strain components considering von Kármán geometric nonlinearity can be expressed more compactly in matrix form as:

$$\varepsilon = \varepsilon^{(0)} + z\varepsilon^{(1)} + z^2\varepsilon^{(2)} + z^3\varepsilon^{(3)} + \varepsilon_{NL} \tag{3}$$

where $\boldsymbol{\varepsilon}^{\top} = \{\varepsilon_{xx}\ \varepsilon_{yy}\ \varepsilon_{zz}\ \gamma_{xy}\ \gamma_{yz}\ \gamma_{xz}\}$ is the strain vector, and the subscript NL stands for nonlinear terms.
Each term of Eq. (3) can be defined as:

$$\begin{aligned} &\boldsymbol{\varepsilon}^{(0)} = \mathbf{D}^{(0)}\mathbf{u}, \quad \boldsymbol{\varepsilon}^{(1)} = \mathbf{D}^{(1)}\mathbf{u}, \quad \boldsymbol{\varepsilon}^{(2)} = \mathbf{D}^{(2)}\mathbf{u} \quad \boldsymbol{\varepsilon}^{(3)} = \mathbf{D}^{(3)}\mathbf{u} \\ &\boldsymbol{\varepsilon}_{NL} = \mathbf{D}^{(M)}\mathbf{u} \circ \mathbf{D}^{(N)}\mathbf{u} \end{aligned} \tag{4}$$

where $\mathbf{u}^{\top} = \{u\ v\ w\ \theta_x\ \theta_y\ \phi_z\ \psi_x\ \psi_y\}$ is the vector of displacement parameters. The kinematic operators $\mathbf{D}^{(0)}$, $\mathbf{D}^{(1)}$, $\mathbf{D}^{(2)}$, $\mathbf{D}^{(3)}$, $\mathbf{D}^{(M)}$, and $\mathbf{D}^{(N)}$ used in Eq. (4) take the form:

$$\mathbf{D}^{(0)} = \begin{bmatrix} \frac{\partial}{\partial x} & 0 & 0 & 0 & 0 & 0 & 0 & 0 \\ 0 & \frac{\partial}{\partial y} & 0 & 0 & 0 & 0 & 0 & 0 \\ 0 & 0 & 0 & 0 & 0 & 0 & 0 & 0 \\ \frac{\partial}{\partial y} & \frac{\partial}{\partial x} & 0 & 0 & 0 & 0 & 0 & 0 \\ 0 & 0 & \frac{\partial}{\partial y} & 0 & 1 & 0 & 0 & 0 \\ 0 & 0 & \frac{\partial}{\partial x} & 1 & 0 & 0 & 0 & 0 \end{bmatrix} \tag{5}$$

$$\mathbf{D}^{(1)} = \begin{bmatrix} 0 & 0 & 0 & \frac{\partial}{\partial x} & 0 & 0 & 0 & 0 \\ 0 & 0 & 0 & 0 & \frac{\partial}{\partial y} & 0 & 0 & 0 \\ 0 & 0 & 0 & 0 & 0 & 2 & 0 & 0 \\ 0 & 0 & 0 & \frac{\partial}{\partial y} & \frac{\partial}{\partial x} & 0 & 0 & 0 \\ 0 & 0 & 0 & 0 & 0 & 0 & 0 & 0 \\ 0 & 0 & 0 & 0 & 0 & 0 & 0 & 0 \end{bmatrix} \tag{6}$$

$$\mathbf{D}^{(2)} = \begin{bmatrix} 0 & 0 & 0 & 0 & 0 & 0 & 0 & 0 \\ 0 & 0 & 0 & 0 & 0 & 0 & 0 & 0 \\ 0 & 0 & 0 & 0 & 0 & 0 & 0 & 0 \\ 0 & 0 & 0 & 0 & 0 & 0 & 0 & 0 \\ 0 & 0 & 0 & 0 & 0 & \frac{\partial}{\partial y} & 0 & 3 \\ 0 & 0 & 0 & 0 & 0 & \frac{\partial}{\partial x} & 3 & 0 \end{bmatrix} \tag{7}$$

$$\mathbf{D}^{(3)} = \begin{bmatrix} 0 & 0 & 0 & 0 & 0 & 0 & \frac{\partial}{\partial x} & 0 \\ 0 & 0 & 0 & 0 & 0 & 0 & 0 & \frac{\partial}{\partial y} \\ 0 & 0 & 0 & 0 & 0 & 0 & 0 & 0 \\ 0 & 0 & 0 & 0 & 0 & 0 & \frac{\partial}{\partial y} & \frac{\partial}{\partial x} \\ 0 & 0 & 0 & 0 & 0 & 0 & 0 & 0 \\ 0 & 0 & 0 & 0 & 0 & 0 & 0 & 0 \end{bmatrix} \tag{8}$$

$$\mathbf{D}^{(M)} = \begin{bmatrix} 0 & 0 & \frac{1}{2}\frac{\partial}{\partial x} & 0 & 0 & 0 & 0 & 0 \\ 0 & 0 & \frac{1}{2}\frac{\partial}{\partial y} & 0 & 0 & 0 & 0 & 0 \\ 0 & 0 & 0 & 0 & 0 & 0 & 0 & 0 \\ 0 & 0 & \frac{\partial}{\partial x} & 0 & 0 & 0 & 0 & 0 \\ 0 & 0 & 0 & 0 & 0 & 0 & 0 & 0 \\ 0 & 0 & 0 & 0 & 0 & 0 & 0 & 0 \end{bmatrix} \tag{9}$$

$$\mathbf{D}^{(N)} = \begin{bmatrix} 0 & 0 & \frac{\partial}{\partial x} & 0 & 0 & 0 & 0 & 0 \\ 0 & 0 & \frac{\partial}{\partial y} & 0 & 0 & 0 & 0 & 0 \\ 0 & 0 & 0 & 0 & 0 & 0 & 0 & 0 \\ 0 & 0 & \frac{\partial}{\partial y} & 0 & 0 & 0 & 0 & 0 \\ 0 & 0 & 0 & 0 & 0 & 0 & 0 & 0 \\ 0 & 0 & 0 & 0 & 0 & 0 & 0 & 0 \end{bmatrix} \tag{10}$$

The constitutive relation of stress can be presented as [18]:

$$\begin{Bmatrix} \sigma_{xx} \\ \sigma_{yy} \\ \sigma_{zz} \\ \sigma_{xy} \\ \sigma_{yz} \\ \sigma_{xz} \end{Bmatrix} = \begin{bmatrix} C_{11} & C_{12} & C_{13} & 0 & 0 & 0 \\ C_{12} & C_{22} & C_{23} & 0 & 0 & 0 \\ C_{13} & C_{23} & C_{33} & 0 & 0 & 0 \\ 0 & 0 & 0 & C_{66} & 0 & 0 \\ 0 & 0 & 0 & 0 & C_{44} & 0 \\ 0 & 0 & 0 & 0 & 0 & C_{55} \end{bmatrix} \begin{Bmatrix} \varepsilon_{xx} \\ \varepsilon_{yy} \\ \varepsilon_{zz} \\ \gamma_{xy} \\ \gamma_{yz} \\ \gamma_{xz} \end{Bmatrix} \tag{11}$$

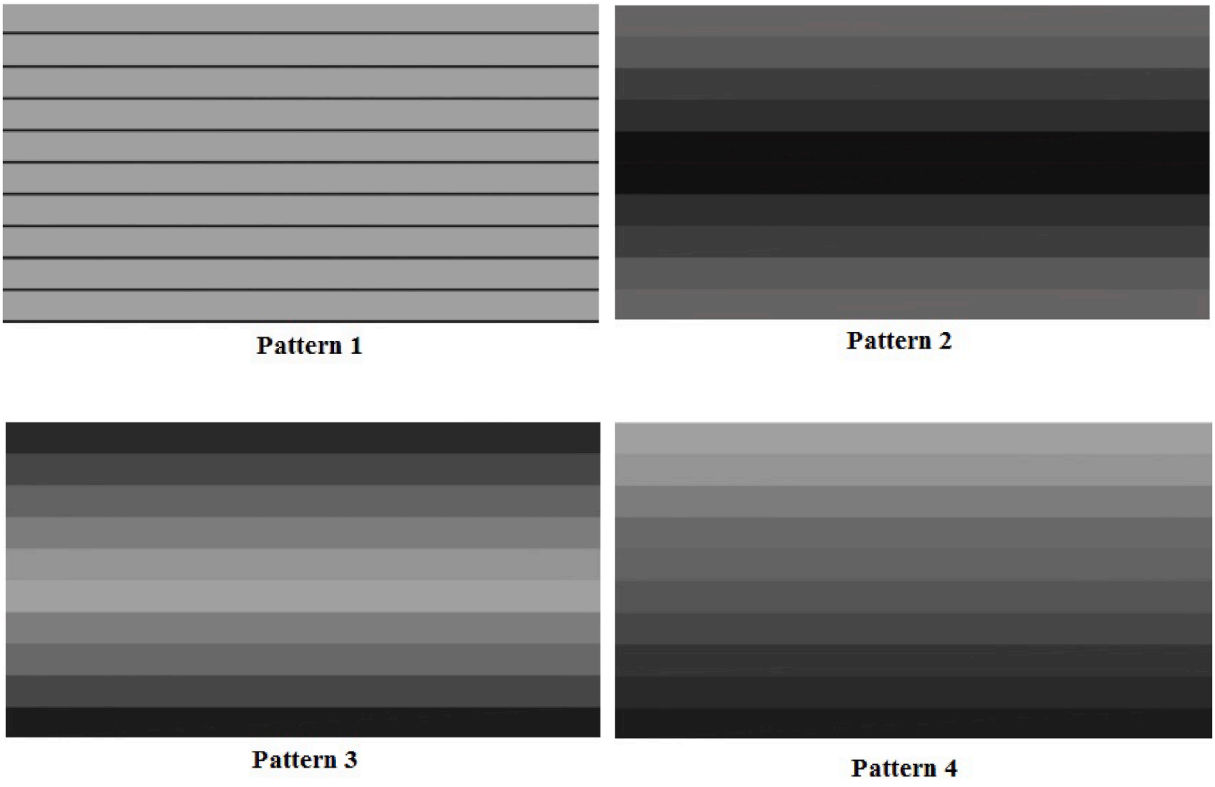

Fig. 1. Different GPL distribution patterns in GPLRC layers.

where C_{ij} denote the components of the stiffness matrix **C** for the GPLRC plate, as described in [13].
The constitutive relation in matrix form can be presented as:

$$\boldsymbol{\sigma} = \mathbf{C}\boldsymbol{\varepsilon} \tag{12}$$

The effective elasticity modulus, density, and Poisson's ratio are computed by employing the Halpin-Tsai micromechanical model and the rule of mixture as addressed in [13]. Graphene platelets (GPLs) are dispersed within epoxy matrix layers. The plate consists of n_l layers of equal thickness, each exhibiting a distinct GPL weight fraction, as shown in Fig. 1. Pattern 1 is an isotropic monotonic multilayer plate case in which the GPLs are distributed regularly. Pattern 2 indicates that the GPL's weight fraction is the highest in the mid-plane and decreases layer by layer when it moves to the top and bottom layers, as shown in Fig. 1. In contrast to Pattern 2, Pattern 3 has both the top and the bottom layers with the maximum weight fraction of GPLs, which it changes to the lowest by moving to the mid-plane. In Pattern 4, the GPL's weight fraction exhibits a non-symmetric linear gradient, with the maximum concentration at the bottom layer and decreasing progressively toward the top surface (see Fig. 1).

The volume fraction functions of these four GPL distribution patterns have been represented as follows [13]:

$$\begin{aligned}
&\text{Pattern 1: } V_{GPL} = V^*_{GPL}\\
&\text{Pattern 2: } V_{GPL} = 2V^*_{GPL}\frac{|2k - n_L - 1|}{n_L}\\
&\text{Pattern 3: } V_{GPL} = V^*_{GPL}\left(1 - \frac{|2k - n_L - 1|}{n_L}\right)\\
&\text{Pattern 4: } V_{GPL} = 2V^*_{GPL}\frac{(2k-1)}{n_l}
\end{aligned} \tag{13}$$

where $k = 1, 2 \ldots, n_l = 10$, and V^*_{GPL} is the total volume fraction of GPL that can be represented as follows:

$$V^*_{GPL} = \frac{W_{GPL}}{W_{GPL} + (\rho_{GPL}/\rho_m)(1 - W_{GPL})} \tag{14}$$

where W_{GPL}, ρ_{GPL} and ρ_m are introduced in the list of symbols.

If the transverse shear stresses, σ_{xz} and σ_{yz}, are required to be vanished on the top and bottom of the plate, as assumed in the Reddy third-order theory [46,47], γ_{xz} and γ_{yz} must be zero at $z = \pm h/2$. This, in turn, leads to two constraints as follows:

$$\psi_x = -\frac{4}{3h^2}\left(\theta_x + \frac{\partial w}{\partial x}\right) - \frac{1}{3}\frac{\partial \phi_z}{\partial x} \tag{15}$$

$$\psi_y = -\frac{4}{3h^2}\left(\theta_y + \frac{\partial w}{\partial y}\right) - \frac{1}{3}\frac{\partial \phi_z}{\partial y} \tag{16}$$

We introduce thickness-integrated stress resultants provided by integration along the thickness of the layer as:

$$\begin{aligned}
\mathbf{N}^{(0)} &= \sum_{k=1}^{n_l}\int_{z_k}^{z_{k+1}} \boldsymbol{\sigma}\, dz = \sum_{k=1}^{n_l}\int_{z_k}^{z_{k+1}} \mathbf{C}^{(k)}(\boldsymbol{\varepsilon}^{(0)} + z\boldsymbol{\varepsilon}^{(1)} + z^2\boldsymbol{\varepsilon}^{(2)} + z^3\boldsymbol{\varepsilon}^{(3)})dz \\
\mathbf{N}^{(1)} &= \sum_{k=1}^{n_l}\int_{z_k}^{z_{k+1}} \boldsymbol{\sigma} z\, dz = \sum_{k=1}^{n_l}\int_{z_k}^{z_{k+1}} \mathbf{C}^{(k)}(z\boldsymbol{\varepsilon}^{(0)} + z^2\boldsymbol{\varepsilon}^{(1)} + z^3\boldsymbol{\varepsilon}^{(2)} + z^4\boldsymbol{\varepsilon}^{(3)})dz \\
\mathbf{N}^{(2)} &= \sum_{k=1}^{n_l}\int_{z_k}^{z_{k+1}} \boldsymbol{\sigma} z^2\, dz = \sum_{k=1}^{n_l}\int_{z_k}^{z_{k+1}} \mathbf{C}^{(k)}(z^2\boldsymbol{\varepsilon}^{(0)} + z^3\boldsymbol{\varepsilon}^{(1)} + z^4\boldsymbol{\varepsilon}^{(2)} + z^5\boldsymbol{\varepsilon}^{(3)})dz \\
\mathbf{N}^{(3)} &= \sum_{k=1}^{n_l}\int_{z_k}^{z_{k+1}} \boldsymbol{\sigma} z^3\, dz = \sum_{k=1}^{n_l}\int_{z_k}^{z_{k+1}} \mathbf{C}^{(k)}(z^3\boldsymbol{\varepsilon}^{(0)} + z^4\boldsymbol{\varepsilon}^{(1)} + z^5\boldsymbol{\varepsilon}^{(2)} + z^6\boldsymbol{\varepsilon}^{(3)})dz
\end{aligned} \tag{17}$$

where n_l considered to be the total number of layers as mentioned earlier, and the generic kth ply is characterized by thickness $h_k = z_{k+1} - z_k$, where z_{k+1}, z_k are the upper and lower bounds. Therefore, the overall thickness can be computed as $h = \sum_{k=1}^{n_l} h_k$. The superscript (k) indicates the $k-$th orthotropic lamina. Therefore, the constitutive equations presented in Eq. (17) in terms of stress resultants are:

$$\begin{Bmatrix} \mathbf{N}^{(0)} \\ \mathbf{N}^{(1)} \\ \mathbf{N}^{(2)} \\ \mathbf{N}^{(3)} \end{Bmatrix} = \begin{bmatrix} \mathbf{A}_0 & \mathbf{A}_1 & \mathbf{A}_2 & \mathbf{A}_3 \\ \mathbf{A}_1 & \mathbf{A}_2 & \mathbf{A}_3 & \mathbf{A}_4 \\ \mathbf{A}_2 & \mathbf{A}_3 & \mathbf{A}_4 & \mathbf{A}_5 \\ \mathbf{A}_3 & \mathbf{A}_4 & \mathbf{A}_5 & \mathbf{A}_6 \end{bmatrix} \begin{Bmatrix} \boldsymbol{\varepsilon}^{(0)} \\ \boldsymbol{\varepsilon}^{(1)} \\ \boldsymbol{\varepsilon}^{(2)} \\ \boldsymbol{\varepsilon}^{(3)} \end{Bmatrix} \tag{18}$$

where

$$\begin{Bmatrix} \mathbf{A}_0 & \mathbf{A}_1 & \mathbf{A}_2 & \mathbf{A}_3 & \mathbf{A}_4 & \mathbf{A}_5 & \mathbf{A}_6 \end{Bmatrix} = \sum_{k=1}^{n_l}\int_{z_k}^{z_{k+1}} \mathbf{C}^{(k)} \begin{Bmatrix} 1 & z & z^2 & z^3 & z^4 & z^5 & z^6 \end{Bmatrix} dz \tag{19}$$

It is good to mention that the the components of the matrix $\mathbf{A}_1$, $\mathbf{A}_3$, and $\mathbf{A}_5$ are equal to zero for isotropic plates and symmetric laminate plates due to the odd function properties in symmetric domains [48].
The variation of the strain energy is the following:

$$\delta U = \int_V \delta\boldsymbol{\varepsilon}^{\top}\boldsymbol{\sigma}\, dV \tag{20}$$

substituting the terms indicated in Eq. (3) into equation Eq. (20) yields:

$$\delta U = \int_V \left(\delta\boldsymbol{\varepsilon}^{(0)} + z\delta\boldsymbol{\varepsilon}^{(1)} + z^2\delta\boldsymbol{\varepsilon}^{(2)} + z^3\delta\boldsymbol{\varepsilon}^{(3)} + \delta\boldsymbol{\varepsilon}_{NL}\right)^{\top}\boldsymbol{\sigma}\, dV \tag{21}$$

using extended form of Eqs. (4) and (21) becomes:

$$\begin{aligned}
\delta U = \int_A \Big[&(\mathbf{D}^{(0)}\delta\mathbf{u})^{\top}\mathbf{N}^{(0)} + (\mathbf{D}^{(1)}\delta\mathbf{u})^{\top}\mathbf{N}^{(1)} + (\mathbf{D}^{(2)}\delta\mathbf{u})^{\top}\mathbf{N}^{(2)} + (\mathbf{D}^{(3)}\delta\mathbf{u})^{\top}\mathbf{N}^{(3)} + \\
&[(\mathbf{D}^{(M)}\delta\mathbf{u})\circ(\mathbf{D}^{(N)}\mathbf{u})]^{\top}\mathbf{N}^{(0)} + [(\mathbf{D}^{(M)}\mathbf{u})\circ(\mathbf{D}^{(N)}\delta\mathbf{u})]^{\top}\mathbf{N}^{(0)}\Big] dA
\end{aligned} \tag{22}$$

The nonlinear strain terms arising from kinematic effects are small compared to those induced by thermal loads; therefore, all nonlinear terms except those influenced by these effects are neglected. For the last two terms of the Eq. (21), the commutative property of the Hadamard product is applied as follows:

$$[(\mathbf{D}^{(M)}\delta\mathbf{u}\circ\mathbf{D}^{(N)}\mathbf{u}]^{\top}\mathbf{N}^{(0)} = (\mathbf{D}^{(M)}\delta\mathbf{u})^{\top}(\mathbf{N}^{(0)}\circ(\mathbf{D}^{(N)}\mathbf{u})) \tag{23}$$

Since a similar definition applies to the other term, Eq. (22) can be further simplified as:

$$\begin{aligned}
\delta U = \int_A \Big[&(\mathbf{D}^{(0)}\delta\mathbf{u})^{\top}\mathbf{N}^{(0)} + (\mathbf{D}^{(1)}\delta\mathbf{u})^{\top}\mathbf{N}^{(1)} + (\mathbf{D}^{(2)}\delta\mathbf{u})^{\top}\mathbf{N}^{(2)} + (\mathbf{D}^{(3)}\delta\mathbf{u})^{\top}\mathbf{N}^{(3)} + \\
&(\mathbf{D}^{(M)}\delta\mathbf{u})^{\top}[\mathbf{N}^{(0)}\circ(\mathbf{D}^{(N)}\mathbf{u})] + (\mathbf{D}^{(M)}\mathbf{u})^{\top}[\mathbf{N}^{(0)}\circ(\mathbf{D}^{(N)}\delta\mathbf{u})]\Big] dA
\end{aligned} \tag{24}$$

Considering the property of the Hadamard product, the following simplification can be made [49]:

$$\mathbf{N}^{(0)} \circ \mathbf{D}^{(N)}\mathbf{u} = \mathbf{N}_0 \mathbf{D}^{(N)}\mathbf{u} \tag{25}$$

where the element-wise multiplication of $\mathbf{N}^{(0)}$ with $\mathbf{D}^{(N)}$ is equivalent to the standard matrix multiplication with $\mathbf{N}_0$ assuming $\mathbf{N}_0$ is a diagonal matrix whose terms on the main diagonal are the components of vector $\mathbf{N}^{(0)}$.
The variation of strain energy can be rewritten as:

$$\begin{aligned}\delta U = \int_A \Big[&(\mathbf{D}^{(0)}\delta\mathbf{u})^\top \mathbf{N}^{(0)} + (\mathbf{D}^{(1)}\delta\mathbf{u})^\top \mathbf{N}^{(1)} + (\mathbf{D}^{(2)}\delta\mathbf{u})^\top \mathbf{N}^{(2)} + (\mathbf{D}^{(3)}\delta\mathbf{u})^\top \mathbf{N}^{(3)} + \\ &(\mathbf{D}^{(M)}\delta\mathbf{u})^\top [\mathbf{N}_0(\mathbf{D}^{(N)}\mathbf{u})] + (\mathbf{D}^{(N)}\delta\mathbf{u})^\top [\mathbf{N}_0(\mathbf{D}^{(M)}\mathbf{u})] \Big] dA\end{aligned} \tag{26}$$

By applying integration by parts, we obtain:

$$\delta U = \int_A (\delta\mathbf{u})^\top \Big[-(\mathbf{D}^{(0)^\top}\mathbf{N}^{(0)}) - (\mathbf{D}^{(1)^\top}\mathbf{N}^{(1)}) - (\mathbf{D}^{(2)^\top}\mathbf{N}^{(2)}) - (\mathbf{D}^{(3)^\top}\mathbf{N}^{(3)}) - \mathbf{D}^{(M)^\top}[\mathbf{N}_0(\mathbf{D}^{(N)}\mathbf{u})] - \mathbf{D}^{(N)^\top}[\mathbf{N}_0(\mathbf{D}^{(M)}\mathbf{u})] \Big] dA + \Gamma_U \tag{27}$$

By using the definition presented in Eq. (18):

$$\begin{aligned}\delta U = \int_A (\delta\mathbf{u})^\top \Big[&-\Big(\mathbf{D}^{(0)^\top}(\mathbf{A}_0\mathbf{D}^{(0)} + \mathbf{A}_1\mathbf{D}^{(1)} + \mathbf{A}_2\mathbf{D}^{(2)} + \mathbf{A}_3\mathbf{D}^{(3)})\Big) \\ &-\Big(\mathbf{D}^{(1)^\top}(\mathbf{A}_1\mathbf{D}^{(0)} + \mathbf{A}_2\mathbf{D}^{(1)} + \mathbf{A}_3\mathbf{D}^{(2)} + \mathbf{A}_4\mathbf{D}^{(3)})\Big) \\ &-\Big(\mathbf{D}^{(2)^\top}(\mathbf{A}_2\mathbf{D}^{(0)} + \mathbf{A}_3\mathbf{D}^{(1)} + \mathbf{A}_4\mathbf{D}^{(2)} + \mathbf{A}_5\mathbf{D}^{(3)})\Big) \\ &-\Big(\mathbf{D}^{(3)^\top}(\mathbf{A}_3\mathbf{D}^{(0)} + \mathbf{A}_4\mathbf{D}^{(1)} + \mathbf{A}_5\mathbf{D}^{(2)} + \mathbf{A}_6\mathbf{D}^{(3)})\Big) \\ &-\mathbf{D}^{(M)^\top}[\mathbf{N}_0(\mathbf{D}^{(N)})] - \mathbf{D}^{(N)^\top}[\mathbf{N}_0(\mathbf{D}^{(M)})] \Big] \mathbf{u}\, dA + \Gamma_U\end{aligned} \tag{28}$$

where Γ_U denotes the boundary terms, which can easily be demonstrated as:

$$\Gamma_U = \left[(\delta\mathbf{u})^\top [\mathbf{N}^{(0)} + \mathbf{N}^{(1)} + \mathbf{N}^{(2)} + \mathbf{N}^{(3)} + \mathbf{N}_0(\mathbf{D}^{(N)}\mathbf{u}) + \mathbf{N}_0(\mathbf{D}^{(M)}\mathbf{u})]\right]_\Gamma \tag{29}$$

3. Lagrange multiplier method (LMM)

The variational statement considering the Lagrange Multiplier Method (LMM) is [44]:

$$\delta U + \delta\Pi_L = 0 \tag{30}$$

where Π_L represents the energy term of the LMM method. The two constraint equations are presented in Eqs. (15) and (16).
The variation of the energy term can be stated as:

$$\delta\Pi_L = \int_A \Big(\delta\boldsymbol{\lambda}^\top(\mathbf{D}_\lambda\mathbf{u}) + (\mathbf{D}_\lambda\delta\mathbf{u})^\top\boldsymbol{\lambda}\Big) dA \tag{31}$$

where $\boldsymbol{\lambda}^\top = \{\lambda_1\ \lambda_2\}$ represents the Lagrange multiplier vector and the operator $\mathbf{D}_\lambda$ is represented as:

$$\mathbf{D}_\lambda = \begin{bmatrix} 0 & 0 & \frac{4}{3h^2}\frac{\partial}{\partial x} & \frac{4}{3h^2} & 0 & \frac{1}{3}\frac{\partial}{\partial x} & 1 & 0 \\ 0 & 0 & \frac{4}{3h^2}\frac{\partial}{\partial y} & 0 & \frac{4}{3h^2} & \frac{1}{3}\frac{\partial}{\partial y} & 0 & 1 \end{bmatrix} \tag{32}$$

4. Penalty method (PM)

The variational statement for the penalty case is given by [44]:

$$\delta U + \delta\Pi_p = 0 \tag{33}$$

The energy functional for the penalty function is given by:

$$\begin{aligned}\Pi_p = \frac{1}{2}\int_A \Bigg[&p_1^2\left(\psi_x + \frac{4}{3h^2}\left(\theta_x + \frac{\partial w}{\partial x}\right) + \frac{1}{3}\frac{\partial\phi_z}{\partial x}\right)^2 + p_2^2\left(\psi_y + \frac{4}{3h^2}\left(\theta_y + \frac{\partial w}{\partial y}\right) + \frac{1}{3}\frac{\partial\phi_z}{\partial y}\right)^2 \\ &+ 2p_1p_2\left(\psi_x + \frac{4}{3h^2}\left(\theta_x + \frac{\partial w}{\partial x}\right) + \frac{1}{3}\frac{\partial\phi_z}{\partial x}\right)\left(\psi_y + \frac{4}{3h^2}\left(\theta_y + \frac{\partial w}{\partial y}\right) + \frac{1}{3}\frac{\partial\phi_z}{\partial y}\right)\Bigg] dA\end{aligned} \tag{34}$$

The variation of Π_p is:

$$\begin{aligned}\delta\Pi_p = \int_A \Bigg[& p_1^2\left(\delta\psi_x + \frac{4}{3h^2}\left(\delta\theta_x + \frac{\partial\delta w}{\partial x}\right) + \frac{1}{3}\frac{\partial\delta\phi_z}{\partial x}\right)\left(\psi_x + \frac{4}{3h^2}\left(\theta_x + \frac{\partial w}{\partial x}\right) + \frac{1}{3}\frac{\partial\phi_z}{\partial x}\right) \\ & + p_2^2\left(\delta\psi_y + \frac{4}{3h^2}\left(\delta\theta_y + \frac{\partial\delta w}{\partial y}\right) + \frac{1}{3}\frac{\partial\delta\phi_z}{\partial y}\right)\left(\psi_y + \frac{4}{3h^2}\left(\theta_y + \frac{\partial w}{\partial y}\right) + \frac{1}{3}\frac{\partial\phi_z}{\partial y}\right) \\ & + p_1 p_2\left(\delta\psi_x + \frac{4}{3h^2}\left(\delta\theta_x + \frac{\partial\delta w}{\partial x}\right) + \frac{1}{3}\frac{\partial\delta\phi_z}{\partial x}\right)\left(\psi_y + \frac{4}{3h^2}\left(\theta_y + \frac{\partial w}{\partial y}\right) + \frac{1}{3}\frac{\partial\phi_z}{\partial y}\right) \\ & + p_1 p_2\left(\delta\psi_y + \frac{4}{3h^2}\left(\delta\theta_y + \frac{\partial\delta w}{\partial y}\right) + \frac{1}{3}\frac{\partial\delta\phi_z}{\partial y}\right)\left(\psi_x + \frac{4}{3h^2}\left(\theta_x + \frac{\partial w}{\partial x}\right) + \frac{1}{3}\frac{\partial\phi_z}{\partial x}\right)\Bigg] dA\end{aligned} \tag{35}$$

If $p_1, p_2 \to \infty$, the constraints are satisfied exactly. The penalized potential, Π_p, is a function of the variables $w, \theta_x, \theta_y, \phi_z, \psi_x$, and ψ_y.

$$\delta\Pi_p = \int_A (\mathbf{D}_p\delta\mathbf{u})^\top \mathbf{P}(\mathbf{D}_p\mathbf{u})\, dA \tag{36}$$

where $\mathbf{D}_p = \mathbf{D}_\lambda$ as presented in Eq. (32) and the penalty parameters can be collected in the matrix $\mathbf{P}$ as:

$$\mathbf{P} = \begin{bmatrix} p_1^2 & p_1 p_2 \\ p_1 p_2 & p_2^2 \end{bmatrix} \tag{37}$$

The finite element method can be applied by employing the standard finite element procedure [50], considering Lagrange interpolating polynomials as:

$$\mathbf{u}_L = \begin{Bmatrix} \mathbf{u} \\ \boldsymbol{\lambda} \end{Bmatrix} = \begin{bmatrix} \mathbf{N}_8 & \mathbf{0} \\ \mathbf{0} & \mathbf{N}_2 \end{bmatrix} \begin{Bmatrix} \bar{\mathbf{u}} \\ \bar{\boldsymbol{\lambda}} \end{Bmatrix} = \mathbf{N}\mathbf{d}_e \tag{38}$$

where $\mathbf{N}$ collects the shape functions [50] and $\mathbf{d}_e$ represents the generalized displacement vector. $\mathbf{N}_8$ is a mainly diagonal $8 \times 8n$ matrix, and analogously $\mathbf{N}_2$ is a mainly diagonal $2 \times 2n$ matrix.
The discretized form of the system is expressed as follows:

$$\begin{aligned}\delta\bar{\mathbf{u}}^\top \Bigg\{ & \int_{A_e} (\mathbf{B}_0^\top\mathbf{A}_0\mathbf{B}_0 + \mathbf{B}_0^\top\mathbf{A}_1\mathbf{B}_1 + \mathbf{B}_0^\top\mathbf{A}_2\mathbf{B}_2 + \mathbf{B}_0^\top\mathbf{A}_3\mathbf{B}_3 + \mathbf{B}_1^\top\mathbf{A}_1\mathbf{B}_0 + \mathbf{B}_1^\top\mathbf{A}_2\mathbf{B}_1 + \mathbf{B}_1^\top\mathbf{A}_3\mathbf{B}_2 + \mathbf{B}_1^\top\mathbf{A}_4\mathbf{B}_3 + \mathbf{B}_2^\top\mathbf{A}_2\mathbf{B}_0 \\ & + \mathbf{B}_2^\top\mathbf{A}_3\mathbf{B}_1 + \mathbf{B}_2^\top\mathbf{A}_4\mathbf{B}_2 + \mathbf{B}_2^\top\mathbf{A}_5\mathbf{B}_3 + \mathbf{B}_3^\top\mathbf{A}_3\mathbf{B}_0 + \mathbf{B}_3^\top\mathbf{A}_4\mathbf{B}_1 + \mathbf{B}_3^\top\mathbf{A}_5\mathbf{B}_2 + \mathbf{B}_3^\top\mathbf{A}_6\mathbf{B}_3 + \mathbf{B}_M^\top\mathbf{N}_0\mathbf{B}_N + \mathbf{B}_M^\top\mathbf{N}_0\mathbf{B}_N) dA_e \Bigg\}\bar{\mathbf{u}} \\ & + \delta\bar{\mathbf{u}}^\top \Bigg\{ \int_{A_e} \mathbf{B}_\lambda^\top\mathbf{N}^{(0)} dA_e \Bigg\}\bar{\boldsymbol{\lambda}} + \delta\bar{\boldsymbol{\lambda}}^\top \Bigg\{ \int_{A_e} \mathbf{N}^{(\mathbf{0})^\top}\mathbf{B}_\lambda dA_e \Bigg\}\bar{\mathbf{u}} = 0\end{aligned} \tag{39}$$

where $\mathbf{B}_0 = \mathbf{D}^{(0)}\mathbf{N}$, $\mathbf{B}_1 = \mathbf{D}^{(1)}\mathbf{N}$, $\mathbf{B}_2 = \mathbf{D}^{(2)}\mathbf{N}$, $\mathbf{B}_\lambda = \mathbf{D}^{(\lambda)}\mathbf{N}$, $\mathbf{B}_M = \mathbf{D}^{(M)}\mathbf{N}$, $\mathbf{B}_N = \mathbf{D}^{(N)}\mathbf{N}$. Eventually, the stiffness matrix for the LMM can be derived as:

$$\begin{aligned}\mathbf{K}_\lambda = \int_{A_e} \Big(& \mathbf{B}_0^\top\mathbf{A}_0\mathbf{B}_0 + \mathbf{B}_0^\top\mathbf{A}_1\mathbf{B}_1 + \mathbf{B}_0^\top\mathbf{A}_2\mathbf{B}_2 + \mathbf{B}_0^\top\mathbf{A}_3\mathbf{B}_3 + \mathbf{B}_1^\top\mathbf{A}_1\mathbf{B}_0 + \mathbf{B}_1^\top\mathbf{A}_2\mathbf{B}_1 + \mathbf{B}_1^\top\mathbf{A}_3\mathbf{B}_2 + \mathbf{B}_1^\top\mathbf{A}_4\mathbf{B}_3 + \mathbf{B}_2^\top\mathbf{A}_2\mathbf{B}_0 \\ & + \mathbf{B}_2^\top\mathbf{A}_3\mathbf{B}_1 + \mathbf{B}_2^\top\mathbf{A}_4\mathbf{B}_2 + \mathbf{B}_2^\top\mathbf{A}_5\mathbf{B}_3 + \mathbf{B}_3^\top\mathbf{A}_3\mathbf{B}_0 + \mathbf{B}_3^\top\mathbf{A}_4\mathbf{B}_1 + \mathbf{B}_3^\top\mathbf{A}_5\mathbf{B}_2 + \mathbf{B}_3^\top\mathbf{A}_6\mathbf{B}_3 + \mathbf{B}_\lambda^\top\mathbf{N}\mathbf{B}_\lambda + \mathbf{B}_\lambda\mathbf{N}^\top\mathbf{B}_\lambda^\top \Big) dA_e\end{aligned} \tag{40}$$

Eq. (39) can also be written in this form:

$$\begin{Bmatrix} \delta\bar{\mathbf{u}} & \delta\bar{\boldsymbol{\lambda}} \end{Bmatrix} \begin{bmatrix} \mathbf{K}_{uu} & \mathbf{K}_{u\lambda} \\ \mathbf{K}_{\lambda u} & \mathbf{0} \end{bmatrix} \begin{Bmatrix} \bar{\mathbf{u}} \\ \bar{\boldsymbol{\lambda}} \end{Bmatrix} = 0 \tag{41}$$

where $\mathbf{K}_{\lambda u} = \mathbf{K}_{u\lambda}^\top$. Here, the finite element implementation for the Penalty function is presented:

$$\begin{aligned}\delta\bar{\mathbf{u}}^\top \Bigg\{ & \int_{A_e} (\mathbf{B}_0^\top\mathbf{A}_0\mathbf{B}_0 + \mathbf{B}_0^\top\mathbf{A}_1\mathbf{B}_1 + \mathbf{B}_0^\top\mathbf{A}_2\mathbf{B}_2 + \mathbf{B}_0^\top\mathbf{A}_3\mathbf{B}_3 + \mathbf{B}_1^\top\mathbf{A}_1\mathbf{B}_0 + \mathbf{B}_1^\top\mathbf{A}_2\mathbf{B}_1 + \mathbf{B}_1^\top\mathbf{A}_3\mathbf{B}_2 + \mathbf{B}_1^\top\mathbf{A}_4\mathbf{B}_3 + \mathbf{B}_2^\top\mathbf{A}_2\mathbf{B}_0 \\ & + \mathbf{B}_2^\top\mathbf{A}_3\mathbf{B}_1 + \mathbf{B}_2^\top\mathbf{A}_4\mathbf{B}_2 + \mathbf{B}_2^\top\mathbf{A}_5\mathbf{B}_3 + \mathbf{B}_3^\top\mathbf{A}_3\mathbf{B}_0 + \mathbf{B}_3^\top\mathbf{A}_4\mathbf{B}_1 + \mathbf{B}_3^\top\mathbf{A}_5\mathbf{B}_2 + \mathbf{B}_3^\top\mathbf{A}_6\mathbf{B}_3 + \mathbf{B}_M^\top\mathbf{N}_0\mathbf{B}_N + \mathbf{B}_N^\top\mathbf{N}_0\mathbf{B}_M + \mathbf{B}_p^\top\mathbf{P}\mathbf{B}_p) dA \Bigg\}\mathbf{u} = 0\end{aligned} \tag{42}$$

Therefore the stiffness matrix $\mathbf{K}_p$ including the Penalty method is:

$$\begin{aligned}\mathbf{K}_p = \int_{A_e} \Big(& \mathbf{B}_0^\top\mathbf{A}_0\mathbf{B}_0 + \mathbf{B}_0^\top\mathbf{A}_1\mathbf{B}_1 + \mathbf{B}_0^\top\mathbf{A}_2\mathbf{B}_2 + \mathbf{B}_0^\top\mathbf{A}_3\mathbf{B}_3 + \mathbf{B}_1^\top\mathbf{A}_1\mathbf{B}_0 + \mathbf{B}_1^\top\mathbf{A}_2\mathbf{B}_1 + \mathbf{B}_1^\top\mathbf{A}_3\mathbf{B}_2 + \mathbf{B}_1^\top\mathbf{A}_4\mathbf{B}_3 + \mathbf{B}_2^\top\mathbf{A}_2\mathbf{B}_0 + \\ & \mathbf{B}_2^\top\mathbf{A}_3\mathbf{B}_1 + \mathbf{B}_2^\top\mathbf{A}_4\mathbf{B}_2 + \mathbf{B}_2^\top\mathbf{A}_5\mathbf{B}_3 + \mathbf{B}_3^\top\mathbf{A}_3\mathbf{B}_0 + \mathbf{B}_3^\top\mathbf{A}_4\mathbf{B}_1 + \mathbf{B}_3^\top\mathbf{A}_5\mathbf{B}_2 + \mathbf{B}_3^\top\mathbf{A}_6\mathbf{B}_3 + \mathbf{B}_p^\top\mathbf{P}\mathbf{B}_p \Big) dA_e\end{aligned} \tag{43}$$

where $\mathbf{B}_p = \mathbf{D}_p\mathbf{N}$.
The well-known elastic constitutive equations accounting for thermal effects, expressed in matrix form, are given by:

$$\boldsymbol{\sigma} = \mathbf{C}\boldsymbol{\varepsilon} - \mathbf{C}\boldsymbol{\alpha}\Delta T \tag{44}$$

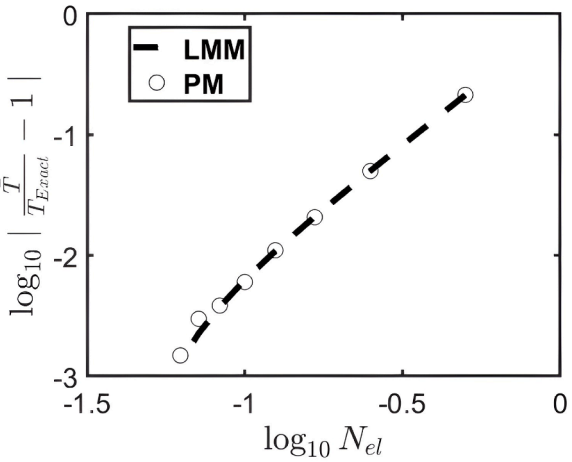

Fig. 2. Convergence plot for a multilayer GPLRC plate employing LMM and PM ($a/b = 1, a/h = 100$, T_{Exact} referred to Ref.[13]).

where $\mathbf{C}$ is introduced in Eq. (11).
For a laminated composite plate with orientation of the layer β, the global thermal expansion matrix $\boldsymbol{\alpha}$ can be derived as:

$$\boldsymbol{\alpha} = \mathbf{T}\boldsymbol{\alpha}_0 \tag{45}$$

where ${\boldsymbol{\alpha}_0}^{\top} = \{\alpha_{xx} \quad \alpha_{yy} \quad \alpha_{zz} \quad \alpha_{xy} \quad \alpha_{yz} \quad \alpha_{xz}\}$, note that only the membrane terms are nonzero and $\mathbf{T}$ is representing a square matrix.

It is necessary to mention that for the thermal buckling analysis, the nonlinear terms affected by thermal loads are taken into account. For this reason, $\mathbf{N}_0$ should be replaced by $\mathbf{H}_d$ which represents the diagonal form of $\mathbf{H}$ for the thermal terms as:

$$\mathbf{H} = \sum_{k=1}^{n_l} \int_{z_k}^{z_{k+1}} \mathbf{C}^{(k)} \boldsymbol{\alpha}^{(k)} \, dz \tag{46}$$

After simplifying the equation terms, the governing equation for determining the critical temperature of the system, T_0 is:

$$\left(\mathbf{K}_T - T_0 \mathbf{K}_G\right)\mathbf{d}_e = \mathbf{0} \tag{47}$$

where $\mathbf{K}_T$ is the stiffness matrix for the thermal buckling of a GTST plate [18]. The stiffness matrices employing the LMM and PM are addressed in Eqs. (40) and (43), respectively. $\mathbf{K}_G$ stands for the geometric stiffness matrix resulting from the thermal force, which takes the form:

$$\mathbf{K}_G = \int_{A_e} \left(\mathbf{B}_M^{\top} \mathbf{H}_d \mathbf{B}_N + \mathbf{B}_N^{\top} \mathbf{H}_d \mathbf{B}_M \right) dA_e \tag{48}$$

where $\mathbf{H}_d$ represents the diagonal form of $\mathbf{H}$.
If the solution of PM is taken into account, $\mathbf{K}_G$ takes the same form as presented in Eq. (48) with the order of $8n \times 8n$ while for the LMM method, the order of the matrices is $10n \times 10n$. In the present study, the finite element method (FEM) has been implemented in an in-house MATLAB code developed entirely from scratch. The initial framework of the code was inspired by the FEM textbook [50]. The computations were performed using MATLAB's built-in eigenvalue solver. A structured mesh consisting of Q4 quadrilateral elements was employed throughout the analysis, with regular rectangular elements as described in the text.

5. Results and discussion

This section presents numerical results of the thermal buckling analysis of the GTST laminated GPLRC plate employing LMM and PM methods. The dimensions of the plate are considered to be $a = b = 1$. The material properties of GPL as a reinforcement and epoxy are given in Table 5. Distribution Patterns 1 to 4 are considered as presented in Fig. 1.

The convergence behavior of the present implementation is thoroughly shown in Fig. 2 (considering $n_l = 10$ for GPLRC plies) for both LMM and PM solutions. The validity of the model is evaluated with respect to the relative error between the numerical solution and the exact value taken from [13], where T_{Exact} refers to the exact value resulting from the analytical computation of the same plate.

Subsequently, a comparison with the literature [51,52], which used a local Kriging meshless method, is shown in Table 2. The average error is demonstrated to be adequate, when compared to both references [51], and [52]. It should be noted that Q4 represents a 4-node finite element as introduced in [50].

Results are presented in terms of the non-dimensional form of the temperature as:

$$T = \alpha_0 T_{cr} \cdot 10^3 \tag{49}$$

Table 1
Material properties of epoxy and GPL.

Material Properties	Epoxy	GPL
E (GPa)	3	1010
ν	0.34	0.186
ρ (kgm^{-3})	200	1060
α (°C^{-1})	$60 \cdot 10^{-6}$	$5 \cdot 10^{-6}$

Table 2
Critical buckling temperature $T = \alpha_0 T_{cr} \cdot 10^3$ for a simply supported GPLRC plate (with $W_{GPL} = 0.3$), using Q4 20×20 elements ($a/b = 1$, $a/h = 100$, and $\nu = 0.3$).

LMM	PM	Ref [51]	Ref [52]	Error (%) - LMM	Error (%) - PM
0.1203	0.1205	0.1265	0.1272	5.08	5

Table 3
Critical buckling temperature $T = \alpha_0 T_{cr} \cdot 10^3$ for a simply supported isotropic plate ($a/b = 1, \alpha_0 = 10^{-6}\,\mathrm{K}^{-1}, E = 10^6\,\mathrm{N/m}^2, \nu = 0.3$).

a/h	Present - LMM			Ref [24]	Error (%)
	16×16	18×18	20×20		
10	10.5	11.05	11.09	11.83	6.25
20	2.716	2.917	2.998	3.089	2.94
100	0.1126	0.1189	0.1203	0.1271	5.35

Table 4
Critical buckling temperature $T = \alpha_0 T_{cr} \cdot 10^3$ of the simply supported isotropic plate ($a/b = 1, \alpha_0 = 10^{-6}\,\mathrm{K}^{-1}, E = 10^6\,\mathrm{N/m}^2, \nu = 0.3$).

a/h	Present - PM			Ref [24]	Error (%)
	16×16	18×18	20×20		
10	10.5	11.63	11.19	11.83	5.40
20	2.798	2.983	3.021	3.089	2.20
100	0.1114	0.1186	0.1205	0.1271	5.19

where α resulted from the rule of mixture [13]. The critical temperature is computed as:

$$T_{cr} = \min(T_0) \tag{50}$$

where T_0 is carried out based on the eigenvalue solution of the Eq. (47). In all the following computations, $N_{el} = 20$ finite elements are considered, given that such many finite elements provide accurate solutions within a reduced computational time.

Validation based on the number of elements, compared to [24], which used the kp-Ritz method, is summarized in Tables 3 and 4 for LMM and Pm methods respectively. Results indicate an acceptable average error compared to the reference [24]. Both tables show a consistent trend with respect to the number of elements; as the number of elements increases, the corresponding values also increase, which is expected and consistent with anticipated behavior. A reduction in error is observed as the plate thickness decreases, corresponding to an increase in the a/h ratio from the thickest to the thinnest configuration examined in the current study.

According to the results obtained from these two tables, PM seems slightly more accurate than LMM when compared to the same from [24].

The effects of the weight fraction of GPLs, represented by W_{GPL}, on the thermal buckling behavior of the GPLRC laminates, considering four distribution patterns, are illustrated in Fig. 3. For this computation, both the LMM and PM methods are considered to assess the validity of the proposed approach. As observed in Fig. 3, dispersing more GPLs in outer layers of the laminate plate, like Patterns 3 and 4, results in higher critical temperature values. This highlights that the outer layers of a laminate contribute most to the bending stiffness because stiffness increases with the distance from the neutral axis, which in turn enhances bending resistance and delays the onset of thermal buckling. In other words, it is attributed to the fact that the outer layers experience the highest thermal stresses due to temperature gradients, and the increased stiffness and thermal conductivity from the GPLs help resist deformation under these conditions.

Fig. 4 illustrates the influence of plate thickness on the critical buckling temperature. As the ratio a/h increases (i.e., as the plate becomes thinner), the plate stiffness in bending decreases, making it more flexible. Consequently, plates with higher slenderness ratios exhibit larger thermal deformations under the same temperature rise. This increased deformability lowers the thermal load required to trigger instability, resulting in a smaller critical buckling temperature compared to thicker (more compact) plates. From

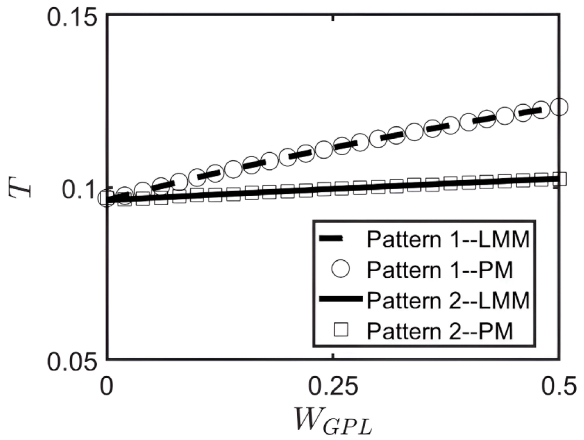

(a)

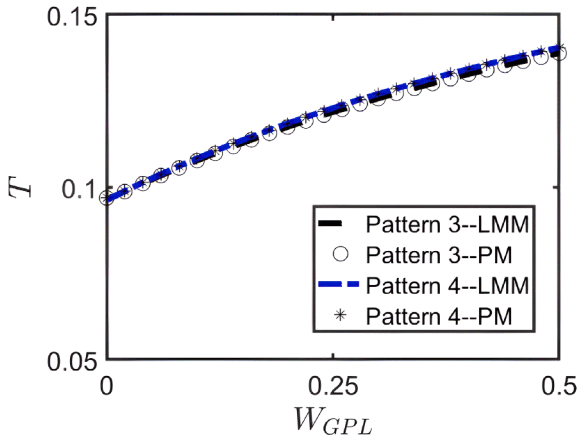

(b)

Fig. 3. Critical buckling temperature ($T = \alpha_0 T_{cr} \cdot 10^3$) vs. GPL weight fraction for a simply supported GPLRC plate: (a) Pattern 1 and Pattern 2, (b) Pattern 3 and Pattern 4 ($a/b = 1, a/h = 100, N_{el} = 20, n_l = 10$).

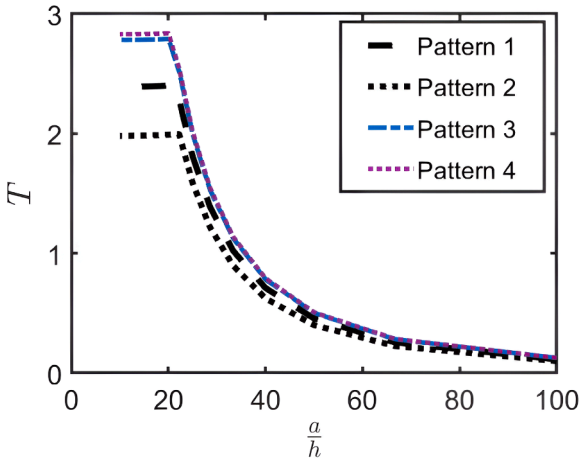

Fig. 4. Critical buckling temperature ($T = \alpha_0 T_{cr} \cdot 10^3$) vs. slenderness ratio a/h for a simply supported GPLRC plate ($a/b = 1, N_{el} = 20, n_l = 10$, $W_{GPL} = 0.3$)).

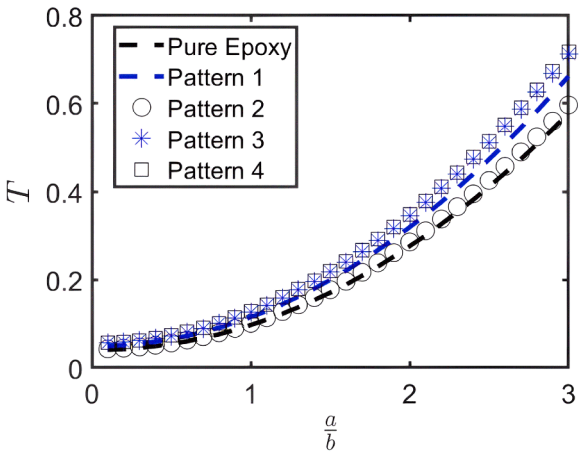

Fig. 5. Critical buckling temperature ($T = \alpha_0 T_{cr} \cdot 10^3$) vs. aspect ratio a/b for a simply supported GPLRC plate considering four patterns of GPL distribution ($N_{el} = 20, n_l = 10, W_{GPL} = 0.3$).

Table 5
Critical buckling temperature ($T = \alpha_0 T_{cr} \cdot 10^3$) vs. geometric ratio a/b for a simply-supported GPLRC plate using 20×20 Q4 elements considering four GPL's distribution patterns ($a/h = 100$, and $W_{GPL} = 0.6$).

	Pure Epoxy		Pattern 1		Pattern 2		Pattern 3		Pattern 4	
a/b	LMM	PM	LMM	PM	LMM	PM	LMM	PM	LMM	PM
0.5	0.0626	0.0632	0.0630	0.0626	0.0627	0.0619	0.0633	0.0633	0.0634	0.0635
1	0.1108	0.1111	0.1115	0.1114	0.1109	0.1105	0.1120	0.1122	0.1121	0.1121
1.5	0.1931	0.1943	0.1943	0.1947	0.1933	0.1929	0.1953	0.1953	0.1954	0.1952

a physical standpoint, a thinner plate stores less bending strain energy for a given in-plane thermal expansion, and the energy balance governing buckling is reached at a lower temperature. It is also worth noting that the influence of ratio a/h on critical buckling temperature becomes significant for ratios more than 25, where shear flexibility reduces the overall bending stiffness and further affects the thermal buckling response. The aspect ratio a/b significantly influences the thermal buckling behavior of laminated composite plates, as shown in Fig. 5. Square plates ($a = b = 1$) generally exhibit higher critical buckling temperatures because their stiffness and constraint conditions are symmetric in both directions, leading to a more balanced resistance to thermal expansion. As the aspect ratio a/b deviates from unity, the plate becomes more compliant along its longer dimension. This directional flexibility reduces the overall bending stiffness and causes non-uniform in-plane thermal stresses, which promote localized deformation and earlier onset of instability. Consequently, plates with higher aspect ratios a/b store less strain energy before reaching the buckling condition, resulting in a lower critical buckling temperature. Therefore, plates with extreme aspect ratios are more prone to thermal buckling due to the combined effects of stiffness asymmetry and uneven stress redistribution.

Table 5 compares the critical buckling temperature parameter T for LMM and PM methods, listing the effects of the aspect ratio a/b considering four distribution patterns. The values were obtained for the simply-supported GPLRC plate using a 20×20 finite element mesh. The results presented in Table 5 demonstrate very good consistency between the two proposed methods, LMM and PM.

Table 6 lists the impact of the GPL's weight fraction on the same parameter when four distribution patterns are considered. As illustrated in Table 6, the results obtained from LMM are in good agreement with those resulting from PM. Study of four distribution patterns in different weight fractions show that placing more reinforcement material in the outer layers (like Pattern 3 and Pattern 4) results in a higher critical buckling temperature. Moreover, as W_{GPL} increases from 0.1 to 0.9, the critical temperature T increases monotonically for all four patterns.

Figs. 6 to 8 illustrate the first ten buckling modes of the structure under study. The associated eigenvalues of each buckling mode λ are noted above each sub-figure. Fig. 6 illustrates the (1–4) buckling modes (eigen modes) of the square GPLRC plate with simply-supported edges using 20×20 Q4, whereas modes (5–8) for the same case are plotted in Fig. 7. Fig. 8 shows modes 9 and 10 for the equivalent scenario.

6. Conclusions

This study successfully analyzed the role of both the Lagrange Multiplier Method (LMM) and the Penalty Method (PM) in thermal buckling behavior of higher-order Graphene Platelet Reinforced Composite (GPLRC) plates using the finite element method (FEM). The General Third-Order Shear Deformation Plate Theory (GTST) was employed to derive the governing equations, combined with the

Table 6
Critical buckling temperature ($T = \alpha_0 T_{cr} \cdot 10^3$) of simply-supported GPLRC square plate vs. GPL's weight fraction (W_{GPL}), using 20×20 Q4 elements considering four GPL's distribution patterns ($a/h = 100$).

	Pattern 1		Pattern 2		Pattern 3		Pattern 4	
$W_{GPL}(\%)$	LMM	PM	LMM	PM	LMM	PM	LMM	PM
0.1	0.1110	0.1111	0.1108	0.1112	0.1110	0.1108	0.1110	0.1107
0.3	0.1111	0.1112	0.1108	0.1109	0.1114	0.1113	0.1114	0.1116
0.6	0.1115	0.1114	0.1109	0.1105	0.1120	0.1122	0.1121	0.1121
0.9	0.1118	0.1118	0.1110	0.1109	0.1127	0.1127	0.1128	0.1129

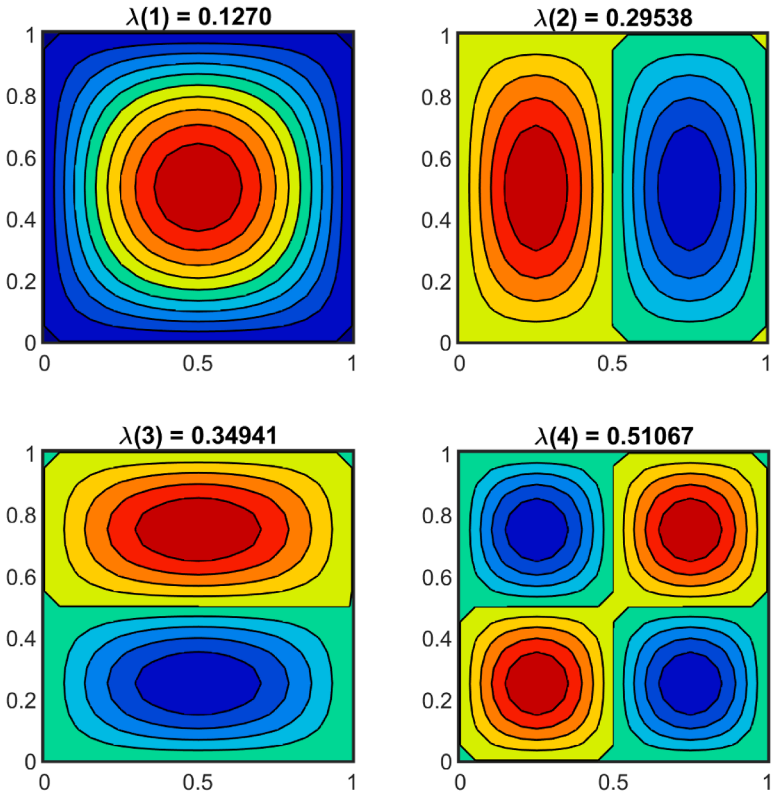

Fig. 6. Buckling modes (1–4) for a simply-supported GPLRC plate ($a = b$), $\frac{a}{h} = 100$, using 20×20 Q4 elements using LMM.

rule of mixtures and Halpin-Tsai micromechanical model, to determine the equivalent material properties of the GPLRC. Four distinct graphene platelet dispersion patterns along the laminated layers were considered. The key findings are summarized as follows:

- The proposed methods enable a streamlined finite element implementation using C^0 approximations, unlike traditional approaches that rely on Hermite interpolation functions, which need C^1 continuity and therefore cause higher computational cost.
- Numerical results exhibit excellent agreement with existing literature, validating the accuracy and stability of both LMM and PM in capturing the complex thermal buckling response of GPLRC plates.
- The computational analysis demonstrates that both methods reliably predict thermal buckling behavior while effectively handling geometric complexities inherent to higher-order shear deformation theories.
- This study offers significant insights into advanced composite modeling, establishing a solid foundation for future developments involving nonlinear effects and experimental validation.

Overall, the research provides a robust computational framework for modeling the thermal behavior of GPLRC laminates, contributing valuable tools for the design and analysis of advanced composite structures.

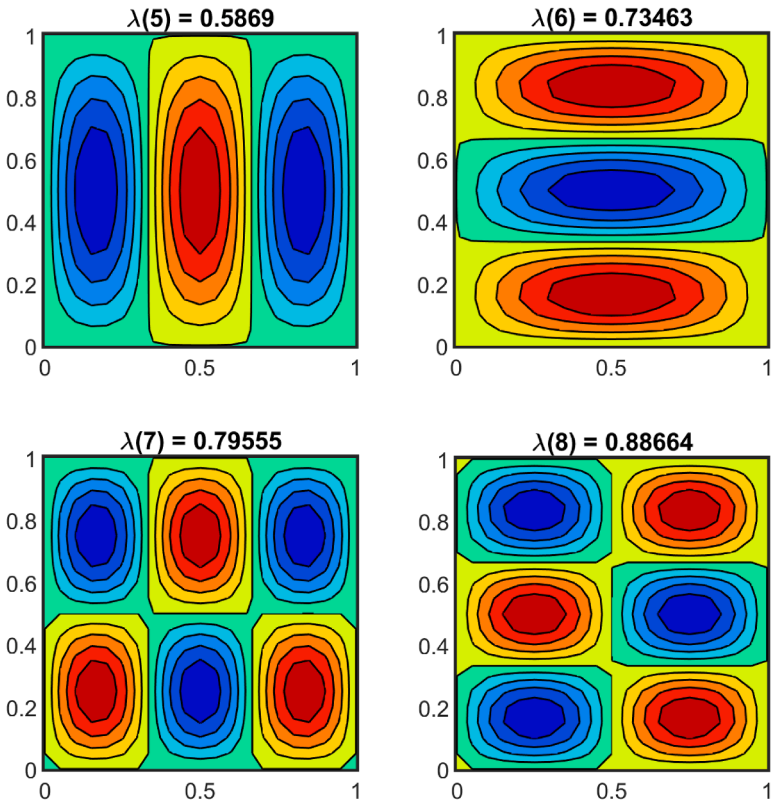

Fig. 7. Buckling modes (5–8) for a simply-supported GPLRC plate ($a = b$), $\frac{a}{h} = 100$, using 20×20 Q4 elements using LMM.

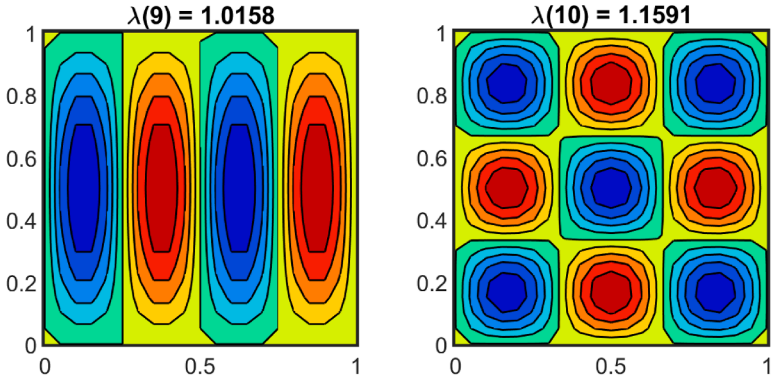

Fig. 8. Buckling modes (9–10) for a simply-supported GPLRC plate ($a = b$), $\frac{a}{h} = 100$, using 20×20 Q4 elements using LMM.

CRediT authorship contribution statement

Saeedeh Qaderi: Writing – review & editing, Writing – original draft, Visualization, Validation, Software, Resources, Methodology, Formal analysis, Data curation, Conceptualization; **Nicholas Fantuzzi:** Writing – review & editing, Visualization, Supervision, Conceptualization; **J.N. Reddy:** Writing – review & editing, Supervision, Investigation, Conceptualization.

Data availability

Data will be made available on request.

Declaration of interests

The authors declare the following financial interests/personal relationships which may be considered as potential competing interests: Authors report financial support was provided by Ministry of University and Research of Italy.

Acknowledgement

This work has been supported by the Ministry of University and Research (MUR), Italy PRIN 2020, project 2020F23HZ7_003 (grant number: J35F22000640001) and PRIN 2022 project 2022YLNJRY (CUP: J53D23002500006), which is funded by the European Union - NextGenerationEU. The authors acknowledge the constructive comments by Mr. Tanmaye Heblekar (doctoral student of Professor J.N. Reddy) in improving the manuscript.

References

[1] W. Zhang, C. Wang, Y. Wang, Thermo-mechanical analysis of porous functionally graded graphene reinforced cylindrical panels using an improved third order shear deformable model, Appl. Math. Model. 118 (2023) 453–473.
[2] E. Zegeye, A.K. Ghamsari, E. Woldesenbet, Mechanical properties of graphene platelets reinforced syntactic foams, Compos. Part B Eng. 60 (2014) 268–273.
[3] S. Qaderi, F. Ebrahimi, Vibration analysis of polymer composite plates reinforced with graphene platelets resting on two-parameter viscoelastic foundation, Eng. Comput. 38 (1) (2022) 419–435.
[4] Y. Wang, Y. Zhou, C. Feng, J. Yang, D. Zhou, S. Wang, Numerical analysis on stability of functionally graded graphene platelets (GPLs) reinforced dielectric composite plate, Appl. Math. Model. 101 (2022) 239–258.
[5] K. Bilisik, M. Akter, Graphene nanoplatelets/epoxy nanocomposites: a review on functionalization, characterization techniques, properties, and applications, J. Reinf. Plast. Compos. 41 (3–4) (2022) 99–129.
[6] G. Shi, S. Araby, C.T. Gibson, Q. Meng, S. Zhu, J. Ma, Graphene platelets and their polymer composites: fabrication, structure, properties, and applications, Adv. Funct. Mater. 28 (19) (2018) 1706705.
[7] S. Qaderi, F. Ebrahimi, V. Mahesh, Free vibration analysis of graphene platelets–reinforced composites plates in thermal environment based on higher-order shear deformation plate theory, Int. J. Aeronaut. Space Sci. 20 (4) (2019) 902–912.
[8] A. Shariati, S. Qaderi, F. Ebrahimi, A. Toghroli, On buckling characteristics of polymer composite plates reinforced with graphene platelets, Eng. Comput. 38 (1) (2022) 513–524.
[9] J.-R. Cho, Buckling analysis of functionally graded GPL-reinforced composite plates under combined thermal and mechanical loads, Materials 18 (3) (2025) 567.
[10] R. Ansari, R. Hassani, J. Torabi, Mixed-type formulation of higher-order shear deformation theory for vibration and buckling analysis of FG-GPLRC plates using VDQFEM, Compos. Struct. 235 (2020) 111738.
[11] H. Mohammadi, Isogeometric thermal buckling analysis of GPL reinforced composite laminated folded plates, Eng. Struct. 255 (2022) 113905.
[12] F. Ebrahimi, S. Qaderi, Stability analysis of embedded graphene platelets reinforced composite plates in thermal environment, Eur. Phys. J. Plus 134 (7) (2019) 349.
[13] S. Qaderi, F. Ebrahimi, M. Vinyas, Dynamic analysis of multi-layered composite beams reinforced with graphene platelets resting on two-parameter viscoelastic foundation, Eur Phys J Plus 134 (7) (2019) 339.
[14] F. Tornabene, M. Bacciocchi, N. Fantuzzi, J.N. Reddy, Multiscale approach for three-phase CNT/polymer/fiber laminated nanocomposite structures, Polym. Compos. 40 (S1) (2019) E102–E126.
[15] A. Haghani, Y. Kiani, Closed form expressions for nonlinear analysis of FG-GPLRC beam under thermal loading: thermal postbuckling and nonlinear bending, Int. J. Struct. Stab. Dyn. 24 (02) (2024) 2450016.
[16] X. Huang, J. Yang, Z. Yang, Thermo-elastic analysis of functionally graded graphene nanoplatelets (GPLs) reinforced closed cylindrical shells, Appl. Math. Model. 97 (2021) 754–770.
[17] P.T. Hung, T. Nguyen-Thanh, P. Phung-Van, H. Nguyen-Gia, Isogeometric vibration of the magneto-electro-elastic sandwich plate with functionally graded carbon nanotube reinforced composite core, J. Adv. Eng. Comput. 7 (3) (2023) 187–203.
[18] J.N. Reddy, Energy Principles and Variational Methods in Applied Mechanics, John Wiley & Sons, 2017.
[19] B. Geier, K. Rohwer, On the analysis of the buckling behaviour of laminated composite plates and shells, Int. J. Numer. Methods Eng. 27 (2) (1989) 403–427.
[20] Y.X. Mukherjee, Z. Xie, A.R. Ingraffea, Delamination buckling of laminated plates, Int. J. Numer. Methods Eng. 32 (6) (1991) 1321–1337.
[21] B. Budiansky, J.W. Hutchinson, A survey of some buckling problems, J. Spacecr. Rockets 40 (6) (2003) 918–923.
[22] J. Sultana, G. Varga, Finite element analysis of post-buckling failure in stiffened panels: a comparative approach, Machines 13 (5) (2025) 373.
[23] E. Riks, Buckling analysis of elastic structures: a computational approach, Adv. Appl. Mech. 34 (1997) 1–76.
[24] X. Zhao, Y.Y. Lee, K.M. Liew, Mechanical and thermal buckling analysis of functionally graded plates, Compos. Struct. 90 (2) (2009) 161–171.
[25] S. Qaderi, M. Ghadiri, M. Najafi, A. Imam, H. Soleimanimehr, Size-dependent nonlinear vibration analysis of cracked graphene-platelets-reinforced-composites (GPLRC) plate under parametric excitation, Commun. Nonlinear Sci. Numer. Simul. 121 (2023) 107232.
[26] C.-K. Chin, F.G.A. Al-Bermani, S. Kitipornchai, Finite element method for buckling analysis of plate structures, J. Struct. Eng. 119 (4) (1993) 1048–1068.
[27] A.K. Noor, W.S. Burton, Three-dimensional solutions for thermal buckling of multilayered anisotropic plates, J. Eng. Mech. 118 (4) (1992) 683–701.
[28] S. Qaderi, F. Ebrahimi, A. Seyfi, An investigation of the vibration of multi-layer composite beams reinforced by graphene platelets resting on two parameter viscoelastic foundation, SN Appl. Sci. 1 (5) (2019) 399.
[29] H. Matsunaga, Thermal buckling of cross-ply laminated composite and sandwich plates according to a global higher-order deformation theory, Compos. Struct. 68 (4) (2005) 439–454.
[30] B. Åesson, Plate Buckling in Bridges and Other Structures, CRC Press, 2014.
[31] J.E. Goldberg, Buckling of multistory buildings, J. Eng. Mech. Div. 91 (1) (1965) 51–70.
[32] D.M. Frangopol, K. Maute, Reliability-based optimization of civil and aerospace structural systems, in: Engineering Design Reliability Handbook, CRC Press, 2004, pp. 559–590.
[33] O.A. Bauchau, J.I. Craig, Structural Analysis: with Applications to Aerospace Structures, 163, Springer Science & Business Media, 2009.
[34] Y. Zhang, J. Teng, J. Huang, K. Zhou, L. Huang, Free and forced vibration analyses of functionally graded graphene-nanoplatelet-reinforced beams based on the finite element method, Materials 15 (17) (2022) 6135.
[35] B.S. Reddy, J.S. Kumar, C.E. Reddy, K.V.K. Reddy, Buckling analysis of functionally graded material plates using higher order shear deformation theory, J. Compos. 2013 (1) (2013) 808764.
[36] S. Qaderi, M. Bacciocchi, N. Fantuzzi, C0 FEM Approximation for the thermal buckling analysis of thin plates: lagrange multiplier and penalty methods, Eur. J. Mech. A/Solids 111 (2025) 105605.
[37] M. Marin, E. Carrera, A.E. Abouelregal, Structural stability study for porous cosserat media, Mech. Adv. Mater. Struct. 31 (15) (2024) 3324–3332.
[38] A. Sadeghirad, A. Vaziri Astaneh, A finite element method with composite shape functions, Eng. Comput. 28 (4) (2011) 389–423.
[39] N.U. Ahmed, P.K. Basu, Higher-order finite element modelling of laminated composite plates, Int. J. Numer. Methods Eng. 37 (1) (1994) 123–139.
[40] Y. Kiani, Free vibration of carbon nanotube reinforced composite plate on point supports using Lagrangian multipliers, Meccanica 52 (6) (2017) 1353–1367.
[41] P.C. Chen, R.L. Ramkumar, Static and dynamic analysis of clamped orthotropic plates using Lagrangian multiplier technique, AIAA J. 25 (2) (1987) 316–323.

[42] C.B. York, F.W. Williams, Buckling analysis of skew plate assemblies: classical plate theory results incorporating Lagrangian multipliers, Comput. Struct. 56 (4) (1995) 625–635.
[43] E.G. Berak, J.C. Gerdeen, A finite element technique for limit analysis of structures (1990).
[44] J.N. Reddy, A penalty plate-bending element for the analysis of laminated anisotropic composite plates, Int. J. Numer. Methods Eng. 15 (8) (1980) 1187–1206.
[45] J. Kim, J. Reddy, A general third-order theory of functionally graded plates with modified couple stress effect and the von Kármán nonlinearity: theory and finite element analysis, Acta Mech. 226 (9) (2015) 2973–2998.
[46] J.N. Reddy, Theory and Analysis of Elastic Plates and Shells, CRC press, 2006.
[47] J.N. Reddy, A simple higher-order theory for laminated composite plates, J. Appl. Mech. 51 (4) (1984) 745–752.
[48] J.N. Reddy, Mechanics of Laminated Composite Plates and Shells: Theory and Analysis, CRC press, 2003.
[49] R.A. Horn, C.R. Johnson, Matrix Analysis, Cambridge university press, 2012.
[50] Ferreira, J.M. António, Fantuzzi, Nicholas, MATLAB Codes for Finite Element Analysis, Second Edition, Springer, 2020.
[51] H. Wu, S. Kitipornchai, J. Yang, Thermal buckling and postbuckling of functionally graded graphene nanocomposite plates, Mater. Des. 132 (2017) 430–441.
[52] L.W. Zhang, P. Zhu, K.M. Liew, Thermal buckling of functionally graded plates using a local Kriging meshless method, Compos. Struct. 108 (2014) 472–492.